A Novel Hybrid Battery Based on a Bidirectional Four-Level Neutral-Point-Clamped DC-DC Power Converter Interfacing

Gabriel Garcia-Rojas,
Sergio Busquets-Monge
Dpt. of Electronic Engineering
Universitat Politècnica de Catalunya
Barcelona, Spain
gabriel.garcia.rojas@upc.edu
sergio.busquets@upc.edu

Àlber Filbà-Martínez
Dpt. of Power Systems
Catalonia Institute for Energy Research
Barcelona, Spain
afilba@irec.cat

Davide Barater
"Enzo Ferrari" Dpt. of Engineering
Università di Modena e R. Emilia
Modena, Italy
davide.barater@unimore.it

***Abstract*—Hybrid batteries combine cells of complementary chemistries, each offering distinct strengths, resulting in battery designs with intermediate features, tailored for each application. With the aim of contributing to the development of modular and scalable hybrid batteries, this paper proposes a novel hybrid battery configuration consisting of two different battery banks, each formed by three series-connected battery modules, and a four-level neutral-point-clamped dc-dc power converter to interface the two battery banks. A suitable operating principle, a modulation strategy, and a closed-loop control are conceived for the proposed system. The power converter enables bidirectional power flow between the battery banks, and it also enables a lossless battery module state of charge balancing, simply by regulating the contribution of each module to the total power transfer, as this is one of the degrees of freedom of the selected multilevel converter topology. Simulation and experimental results verify the feasibility and good performance of the proposed system, demonstrating a substantial regulation margin of battery module currents, even at high modulation index values.**

***Index Terms*—DC-DC power conversion, hybrid battery, multilevel, neutral-point clamped.**

I. Introduction

Batteries have become a fundamental technology for the storage of electrical energy in our society and, as such, the quest to improve their performance is growing. Each battery cell chemistry offers unique features. For instance, while some may present a high power density, others present a high energy density. Ideally, each application requires a specific balance of these different features. While the development of a tailored battery cell chemistry for each application would not be viable, it is possible to combine a few highly optimized and inexpensive battery cells in the right proportion to form a hybrid battery with intermediate features. This allows battery manufacturers to take full advantage of economies of scale resulting in a better final product at a lower cost [1], [2].

There are two main hybrid battery categories based on how the cells are combined: direct connection of the individual cells and power-converter based interfacing. Direct connection is simple and inexpensive but it requires cell voltage curve compatibility, thus limiting the range of candidate cell chemistries. The latter, on the other hand, requires the inclusion of one or more power converters. While this increases the complexity, cost, volume, and weight, it enables the use of a broad range of cell chemistries. Although individual cells could be interconnected using one power converter per cell, known cell chemistries have low cell voltages and this approach would require a large amount of power converters. Additionally, multiple cells are often connected typically in series and in parallel to create high-voltage, high-current battery modules. Then, these battery modules are interconnected again in series and in parallel to form a battery bank with even higher output voltage and current capability. Therefore, a hybrid battery can be configured with existing banks of battery modules, with a single multilevel power converter [3] to interface them, leading to a modular and scalable hybrid battery design approach.

In [4], one such hybrid battery is presented, with two battery banks formed by two series-connected modules and a two-leg three-level neutral-point-clamped (NPC) dc-dc converter interfacing the two banks. With the aim of contributing to the development of such modular and scalable hybrid batteries, this paper proposes the extension of this system to four levels. The system under study consists of two battery banks formed by three series-connected battery modules, and an interfacing two-leg four-level NPC dc-dc converter. The development of a modulation and closed-loop control to independently regulate each battery module current in the interfacing of both battery banks is specially challenging. This regulation is highly desirable, as it allows the balancing of the state-of-charge (SoC) of the battery modules, simply by regulating the power contribution of each module, without incurring in the losses associated to a dedicated SoC balancing circuitry.

The conceived hybrid battery minimizes power processing losses by connecting the load directly to one of the battery banks. This is a major advantage over other state-of-the-art

This publication is part of Grant PID2022-138384NB-I00, funded by MICIU/AEI/10.13039/501100011033 and by ERDF/EU.

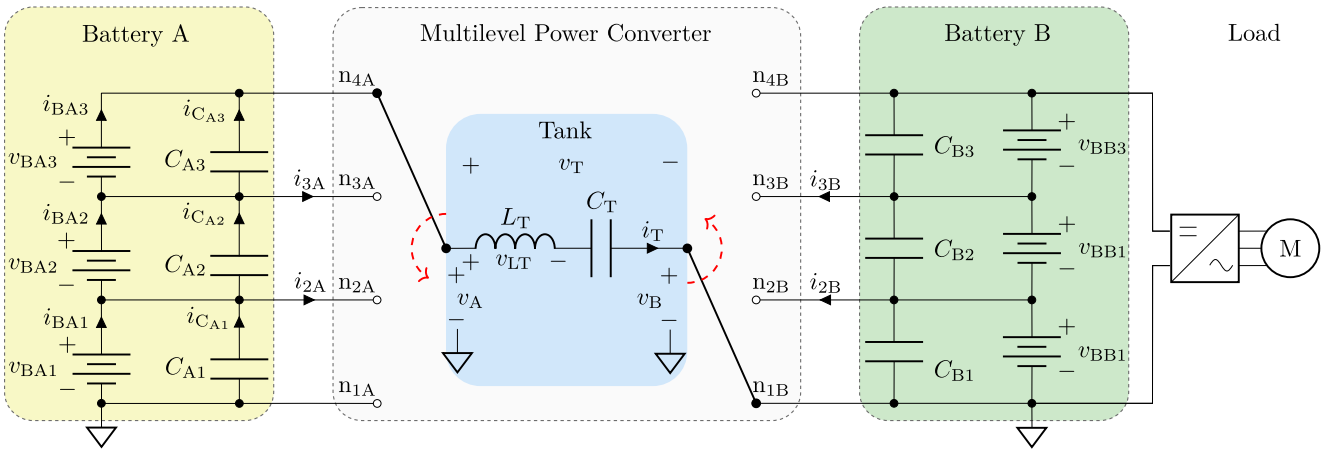

Fig. 1. Proposed four-level NPC hybrid-battery topology, where each battery bank is formed by three battery modules connected in series.

multilevel-based hybrid batteries, where every battery module is connected to the load through power devices [5], [6].

The paper is organized as follows. Section II presents the proposed hybrid battery topology. Section III presents the modulation strategy and control conceived to operate the multilevel power converter. Section IV presents simulation and experimental results validating the feasibility and good performance of the proposed hybrid battery. Finally, Section V outlines the conclusions.

II. Proposed Topology and Operating Principle

The proposed topology is presented in Fig. 1. Two different battery banks, each utilizing different battery chemistries, form the hybrid battery. The battery banks, formed by three series-connected modules, are interfaced through a multilevel power converter consisting of two NPC legs and a LC tank. Each module features a parallel capacitor. The function of these capacitors is to deliver the high-frequency current components required by the NPC-leg operation, and therefore should be placed close to the NPC converter. The NPC legs are modeled as single-pole multiple-throw switches. The return path for the tank current i_{T} is indicated by the ground symbols on both battery banks. In this case, it is connected to the first dc-link point in both battery banks, $\mathrm{n_{1A}}$ and $\mathrm{n_{1B}}$ respectively. The return path can be connected to any of the dc-link points of each battery and they can differ, only affecting the dc component of the tank voltage. The load, illustrated as a motor drive in the figure, is directly powered by battery B.

The power flow between the batteries is controlled by the voltages v_{A} and v_{B}, synthesized by the NPC legs. The rms value of the fundamental component of these voltages, V_{A} and V_{B}, the relative phase shift φ between them, and the tank inductance define the rms value of the fundamental component of the current flowing through the tank, I_{T}. The capacitor C_{T} blocks any dc component of the tank voltage v_{T}. Therefore, the active power exchanged between the batteries can be expressed as

$$P_{\mathrm{A}} = -P_{\mathrm{B}} = V_{\mathrm{A}} \cdot I_{\mathrm{T}} \cdot \cos(\beta - \varphi) = \frac{V_{\mathrm{A}} \cdot V_{\mathrm{B}} \cdot \sin(\varphi)}{w \cdot L_{\mathrm{T}}}, \quad (1)$$

where P_{A} is defined as the sum of the active power delivered by the battery modules of bank A, $P_{\mathrm{A1}} + P_{\mathrm{A2}} + P_{\mathrm{A3}}$, φ is the phase shift of V_{A} with respect to V_{B}, β is the angle of I_{T} with respect to V_{B}, and w is the angular frequency of the fundamental component of v_{A} and v_{B}.

As the phase shift increases, so does the reactive power delivered by side A

$$Q_{\mathrm{A}} = V_{\mathrm{A}} \cdot I_{\mathrm{T}} \cdot \sin(\beta - \varphi) = \frac{V_{\mathrm{A}}^2 - V_{\mathrm{A}} \cdot V_{\mathrm{B}} \cdot \cos(\varphi)}{w \cdot L_{\mathrm{T}}} \quad (2)$$

and side B

$$Q_{\mathrm{B}} = -V_{\mathrm{B}} \cdot I_{\mathrm{T}} \cdot \sin(\beta - \varphi) = \frac{V_{\mathrm{B}}^2 - V_{\mathrm{B}} \cdot V_{\mathrm{A}} \cdot \cos(\varphi)}{w \cdot L_{\mathrm{T}}}. \quad (3)$$

Reactive power does not contribute to the power transfer between battery banks, as it represents an energy flowing back and forth between the tank and the batteries. However, as it will be seen in the next Section, it can be used to redistribute the battery module currents.

The active power flow discussed above is illustrated in Fig. 2, where the multilevel dc-dc converter extracts active power P_{A1}, P_{A2}, and P_{A3} from the side-A battery modules and delivers the aggregated power $P_{\mathrm{A}} = P_{\mathrm{A1}} + P_{\mathrm{A2}} + P_{\mathrm{A3}}$ to the battery bank B: P_{B1} toward module BB1, P_{B2} toward module BB2, and P_{B3} toward module BB3. Finally, a load consuming P_{L} is fed from battery B. In this case, $P_{\mathrm{A1}} = P_{\mathrm{A2}} = P_{\mathrm{A3}}$ and $P_{\mathrm{B1}} = P_{\mathrm{B2}} = P_{\mathrm{B3}}$. Thus, every module within a given bank is delivering/receiving the same amount of power to/from the power converter. With the proposed operating principle, the system can adjust the amount of power transferred between the battery banks. Additionally, the proposed system can also modify the contribution of each individual module to this power exchange, as illustrated in Fig. 3 and explained in the following Section.

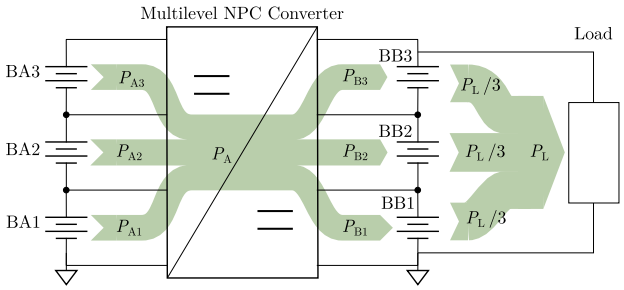

Fig. 2. Power flow across the hybrid battery while feeding a load, under a balanced module power contribution within each bank.

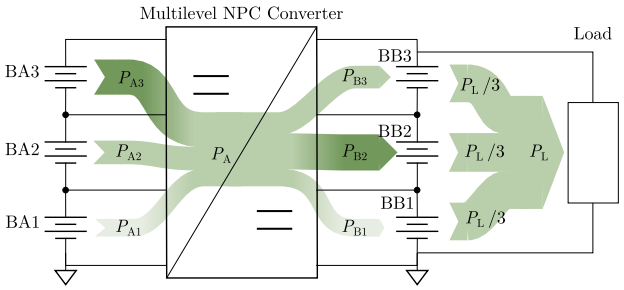

Fig. 3. Power flow across the hybrid battery while feeding a load, under an unbalanced module power contribution within each bank.

III. Proposed Modulation and Control Strategy

This section presents the modulation strategy required for the correct operation of the power converter. For the sake of simplicity, and due to symmetry the analysis is carried out only in side A in Fig. 1. The analysis in side B is analogous. Fig. 4 presents the voltage pattern v_{A} to be generated through the operation of the NPC leg [7]. Typically, $\alpha_{\mathrm{a1}} = \alpha_{\mathrm{b1}} = \alpha_{\mathrm{c1}} = \alpha_{\mathrm{d1}} = \alpha_1$ and $\alpha_{\mathrm{a2}} = \alpha_{\mathrm{b2}} = \alpha_{\mathrm{c2}} = \alpha_{\mathrm{d2}} = \alpha_2$ to force quarter-wave symmetry, eliminating even-order harmonics and providing waveform simplicity. In this case, the rms value of the fundamental component of the leg output voltage depends on α_1 and α_2 as follows:

$$V_{\mathrm{A}} = \frac{2\sqrt{2}V_{\mathrm{dcA}}}{3\pi} \cdot [\sin(\alpha_1) + \sin(\alpha_2) - 0.5], \tag{4}$$

where $V_{\mathrm{dcA}} = v_{\mathrm{BA1}} + v_{\mathrm{BA2}} + v_{\mathrm{BA3}}$ is the total dc-link voltage of battery bank A.
In this case, the modulation index can be defined as

$$m_{\mathrm{A}} = \frac{V_{\mathrm{A}}}{V_{\mathrm{dcA}}/\sqrt{6}} = \frac{4}{\sqrt{3}\pi} \cdot [\sin(\alpha_1) + \sin(\alpha_2) - 0.5], \tag{5}$$

where the modulation index reaches a maximum value of $2\sqrt{3}/\pi \approx 1.1$ for $\alpha_1 = \alpha_2 = \pi/2$.

Let us now analyze the effect of the NPC leg operation on the battery current balance. From Fig. 1, applying Kirchhoff's current law at the dc-link node $\mathrm{n_{2A}}$ and dc-link node $\mathrm{n_{3A}}$

$$\begin{aligned} i_{\mathrm{2A}} &= i_{\mathrm{BA1}} + i_{\mathrm{C_{A1}}} - i_{\mathrm{BA2}} - i_{\mathrm{C_{A2}}} \\ i_{\mathrm{3A}} &= i_{\mathrm{BA2}} + i_{\mathrm{C_{A2}}} - i_{\mathrm{BA3}} - i_{\mathrm{C_{A3}}}. \end{aligned} \tag{6}$$

On average over the switching cycle

$$\begin{aligned} I_{\mathrm{2A}} &= I_{\mathrm{BA1}} - I_{\mathrm{BA2}} \\ I_{\mathrm{3A}} &= I_{\mathrm{BA2}} - I_{\mathrm{BA3}}, \end{aligned} \tag{7}$$

which indicates that the average neutral-point current I_{2A} is responsible for the imbalance between the battery currents I_{BA1} and I_{BA2}, and that the average neutral-point current I_{3A} is responsible for the imbalance between the battery currents I_{BA2} and I_{BA3}; i.e., forcing $I_{\mathrm{2A}} = 0$ and $I_{\mathrm{3A}} = 0$ balances all the battery currents.

Fig. 4 includes a plot of the fundamental component (h1) of the tank current $i_{\mathrm{T,h1}}$, decomposed into a component in phase with the fundamental component of v_{A} ($i^{\mathrm{P}}_{\mathrm{T,h1}}$, responsible for the active power transfer) and a component in quadrature ($i^{\mathrm{Q}}_{\mathrm{T,h1}}$, responsible for the reactive power transfer.) The charge drawn from (positive colored areas) or injected into (negative colored areas) the dc-link node $\mathrm{n_{2A}}$ is shown in yellow, while the charge drawn/injected from/into node $\mathrm{n_{3A}}$ is shown in green.

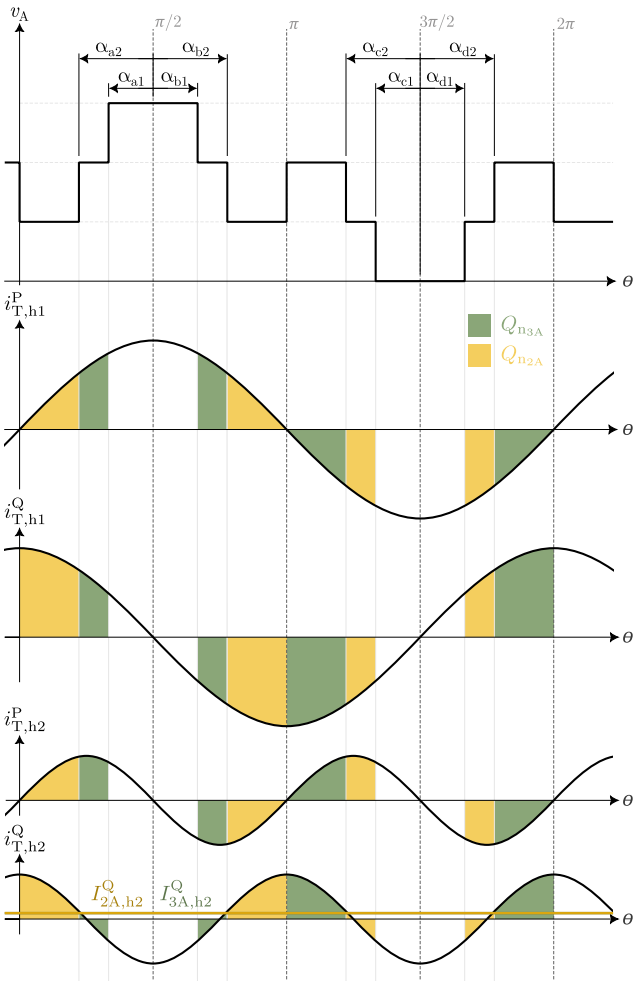

Fig. 4. Four-level modulation pattern ensuring zero average neutral-point currents during converter-leg operation [7].

In Fig. 4, with $\alpha_{\mathrm{a1}} = \alpha_{\mathrm{b1}} = \alpha_{\mathrm{c1}} = \alpha_{\mathrm{d1}} = \alpha_1$ and $\alpha_{\mathrm{a2}} = \alpha_{\mathrm{b2}} = \alpha_{\mathrm{c2}} = \alpha_{\mathrm{d2}} = \alpha_2$, both the charge from node $\mathrm{n_{2A}}$ and

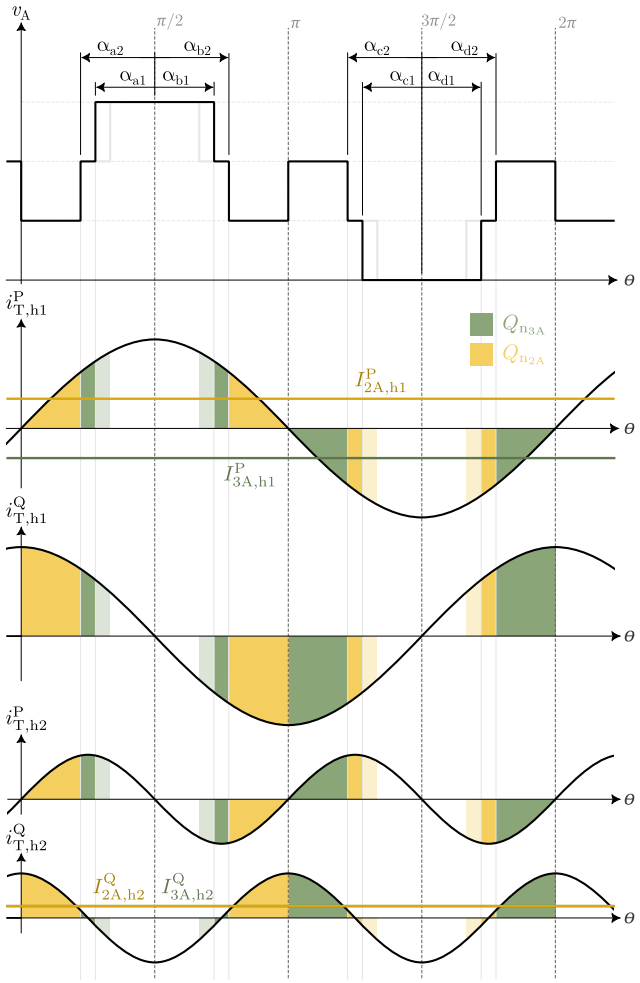

Fig. 5. Proposed modification of the modulation leveraging the in-phase current component.

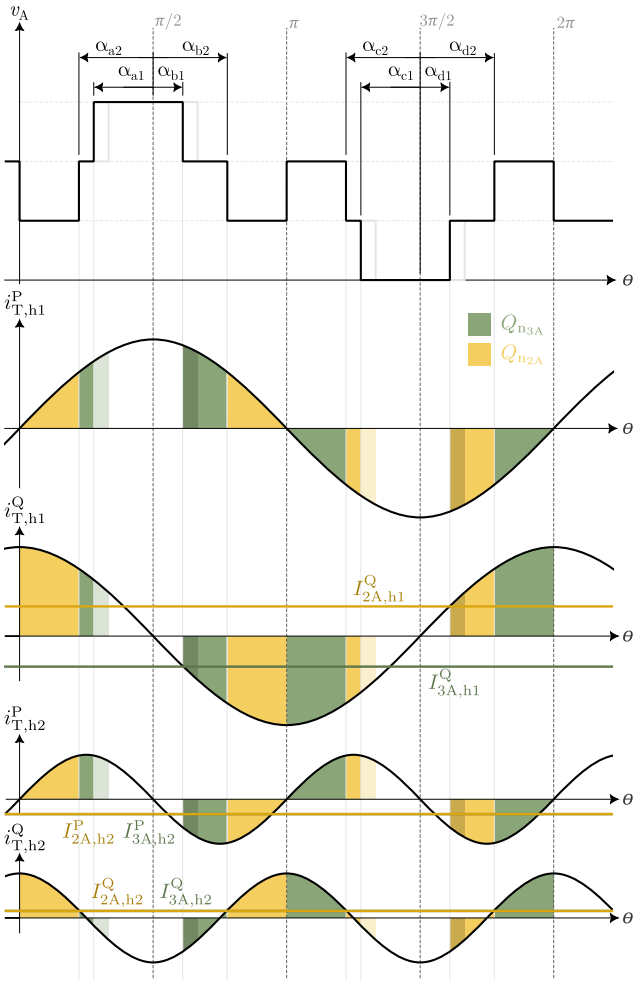

Fig. 6. Proposed modification of the modulation leveraging the in-quadrature current component.

the charge from node $\mathrm{n_{3A}}$ cancel out in $i^{\mathrm{Q}}_{\mathrm{T,h1}}$. If, in addition, α_1 and α_2 verify [7]

$$\sin(\alpha_1) - 2 \cdot \sin(\alpha_2) + 1 = 0, \tag{8}$$

then both charges also cancel out in $i^{\mathrm{P}}_{\mathrm{T,h1}}$. This means that, in the absence of other significant harmonics, $I_{\mathrm{2A}} = 0$ and $I_{\mathrm{3A}} = 0$ and that all three battery modules in this battery bank will feature the same current, ideal for a balanced charging or discharging of these battery modules.

Fig. 4 also includes a plot of the second harmonic (h2) of the tank current $i_{\mathrm{T,h2}}$. Under the conditions described above, the charge exchange due to the second harmonic of the tank current only cancels out for the in-phase component ($i^{\mathrm{P}}_{\mathrm{T,h2}}$) but not necessarily for the in-quadrature component ($i^{\mathrm{Q}}_{\mathrm{T,h2}}$) and, therefore, the battery currents could not be balanced. However, as the generated leg output voltages exhibit quarter-wave symmetry, the second harmonic of the tank current should be negligible. It should be noted that any non-idealities in the output voltages–for example due to any difference in the battery-module voltages or due to the blanking time required by the transistors–will affect this component and should be compensated for by a closed-loop control. The effect of the second harmonic in the power converter operation will be further discussed in Section IV. In the present study, all the other harmonics of i_{T} are neglected.

It may be necessary to introduce an imbalance in the battery module currents to, for instance, equalize their SoC. This can be done by modifying the width and/or position of the positive and negative pulses of v_{A} in correlation with $i^{\mathrm{P}}_{\mathrm{T,h1}}$ and $i^{\mathrm{Q}}_{\mathrm{T,h1}}$. Several strategies are possible. Here, for the sake of simplicity, a simple strategy will be considered: to modify only the positive pulse defined by α_{a1} and α_{b1} or to modify the negative pulse defined by α_{c1} and α_{d1}. For instance, in the first half of Fig. 5, the width of the positive pulse is increased. The green areas still cancel out in $i^{\mathrm{Q}}_{\mathrm{T,h1}}$, but they no longer cancel out in $i^{\mathrm{P}}_{\mathrm{T,h1}}$, introducing an $I_{\mathrm{3A}} < 0$ that will force $I_{\mathrm{BA2}} < I_{\mathrm{BA3}}$. In the second half of this figure, the width of the negative pulse is increased. In this case, the yellow areas still cancel out in $i^{\mathrm{Q}}_{\mathrm{T,h1}}$, but they no longer cancel out in $i^{\mathrm{P}}_{\mathrm{T,h1}}$, introducing an $I_{\mathrm{2A}} > 0$ that will force $I_{\mathrm{BA1}} > I_{\mathrm{BA2}}$.

In Fig. 6, the positive pulse is moved left. The green areas

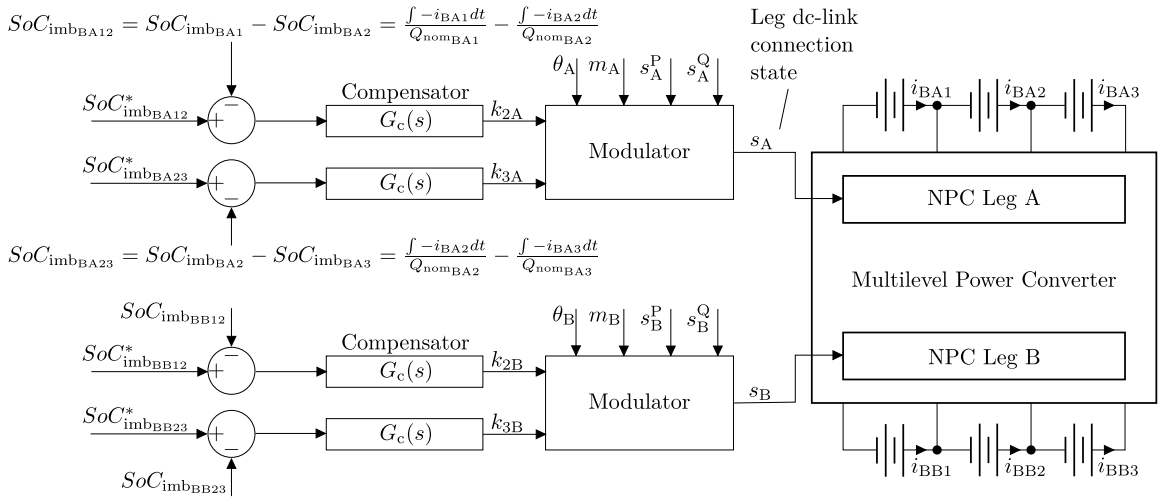

Fig. 7. SoC closed-loop control block diagram of a four-level hybrid battery.

approximately cancel out in $i_{\mathrm{T,h1}}^{\mathrm{P}}$, but they no longer cancel out in $i_{\mathrm{T,h1}}^{\mathrm{Q}}$, introducing an $I_{3\mathrm{A}} < 0$ that will force $I_{\mathrm{BA2}} < I_{\mathrm{BA3}}$. This figure also shows the effect of moving the position of the negative pulse, in this case to the left. The yellow areas approximately cancel out in $i_{\mathrm{T,h1}}^{\mathrm{P}}$, but they no longer cancel out in $i_{\mathrm{T,h1}}^{\mathrm{Q}}$, introducing an $I_{2\mathrm{A}} > 0$ that will force $I_{\mathrm{BA1}} > I_{\mathrm{BA2}}$.

The waveform modifications presented in Figs. 5 and 6 cause the generation of a second current harmonic within the tank current. This harmonic introduces additional unwanted average currents in the neutral points. However, simulations and experimental results indicate that the magnitude of the second harmonic remains low and does not significantly impact the converter operation.

Therefore, the imbalance of the battery currents can be controlled through the fundamental component of the tank current associated to the active and reactive power being transferred, by modifying the width and/or the position of the positive and negative pulses of v_{A}.

Fig. 7 shows a possible closed-loop control to balance the individual SoCs of each battery module based on this principle, where $SoC_{\mathrm{imb_{BA12}}} = SoC_{\mathrm{imb_{BA1}}} - SoC_{\mathrm{imb_{BA2}}}$ is the imbalance between the SoC of battery module 1 and battery module 2 of side A, $SoC_{\mathrm{imb_{BA23}}} = SoC_{\mathrm{imb_{BA2}}} - SoC_{\mathrm{imb_{BA3}}}$ is the the imbalance between the SoC of battery module 2 and battery module 3 of side A, Q_{nom_x} is the nominal capacity of module x, and $s(t) \in 1, 2, 3, 4$. A proportional gain in $G_{\mathrm{c}}(s)$ suffices for a successful implementation.

To determine s_{A} in the modulator block of Fig. 7, it is necessary to first determine the switching angles with

$$\begin{aligned}
\alpha_{\mathrm{a1}} &= \alpha_1 \cdot [1 + k_{3\mathrm{A}} \cdot (s_{\mathrm{A}}^{\mathrm{P}} + s_{\mathrm{A}}^{\mathrm{Q}})] \\
\alpha_{\mathrm{b1}} &= \alpha_1 \cdot [1 + k_{3\mathrm{A}} \cdot (s_{\mathrm{A}}^{\mathrm{P}} - s_{\mathrm{A}}^{\mathrm{Q}})] \\
\alpha_{\mathrm{c1}} &= \alpha_1 \cdot [1 + k_{2\mathrm{A}} \cdot (-s_{\mathrm{A}}^{\mathrm{P}} - s_{\mathrm{A}}^{\mathrm{Q}})] \\
\alpha_{\mathrm{d1}} &= \alpha_1 \cdot [1 + k_{2\mathrm{A}} \cdot (-s_{\mathrm{A}}^{\mathrm{P}} + s_{\mathrm{A}}^{\mathrm{Q}})] \\
\alpha_{\mathrm{a2}} &= \alpha_{\mathrm{b2}} = \alpha_{\mathrm{c2}} = \alpha_{\mathrm{d2}} = \alpha_2,
\end{aligned} \tag{9}$$

where α_1 and α_2 can be obtained from (5) and (8), $s_{\mathrm{A}}^{\mathrm{P}}$ is the sign of active power, and $s_{\mathrm{A}}^{\mathrm{Q}}$ is the sign of the reactive power. If it is desired to restrict the control action to the active power, $s_{\mathrm{A}}^{\mathrm{Q}}$ has to be set to zero in (9). Alternatively, if it is desired to restrict the control action to the reactive power, $s_{\mathrm{A}}^{\mathrm{P}}$ has to be set to zero in (9). The value of the control effort variables $k_{2\mathrm{A}}$ and $k_{3\mathrm{A}}$ may need to be restricted to avoid reaching unfeasible α_1 switching angles outside the range [0, α_2]. Finally, the converter's control strategy and operating principle are compatible with battery banks having different total dc-link voltages, and can be extended to systems with an unequal number of levels on each side.

IV. Simulation and Experimental Results

A switching model of the system described in Fig. 1 has been implemented in MATLAB-Simulink to analyze the performance of the proposed hybrid battery system, where the four-level system is composed of three battery modules on each side. For convenience and simplicity, the same battery module is used in sides A and B. The selected battery module has been modeled in [8]. The converter legs are modeled as ideal single-pole multiple-throw switches. The load model is simplified to a single resistor with value R_{L}. Table I presents the rest of the system parameters and operating conditions, which are the same for both the simulation and the experimental tests.

The first test is performed under open-loop control, with $k_{2\mathrm{A}} = k_{3\mathrm{A}} = k_{2\mathrm{B}} = k_{3\mathrm{B}} = 0$. Fig. 9 shows a few switching cycles of the simulated NPC legs output voltages, the tank current and the battery module currents from both battery banks. The modulation pattern ensures the same average value of the battery module currents within each battery bank, even when operating in open loop, therefore achieving a balanced operation.

A hardware prototype of the proposed hybrid battery has also been implemented, with four-level active NPC legs built with 100 V metal-oxide-semiconductor field-effect transistors,

TABLE I
SIMULATION AND EXPERIMENTAL PARAMETERS AND CONDITIONS

Battery parameters	**Symbol**	**Value**
Nominal voltage	V_{nom}	47 V
Nominal capacity	Q_{nom}	4.3 A h
Battery cell model	Samsung ICR18650-22P	
Battery module configuration	13S2P	
Hybrid topology parameters	**Symbol**	**Value**
Parallel capacitor	C_{A1}, C_{A2}, C_{A3}	320 µF
	C_{B1}, C_{B2}, C_{B3}	320 µF
Tank inductor	L_{T}	94 µH
Tank capacitor	C_{T}	30 µF
Tank parasitic resistance	R_{T}	10 mΩ
Load	R_{L}	22 Ω
Converter modulation and control parameters	**Symbol**	**Value**
Modulation index	m_{A}	0.9
	m_{B}	0.9
Phase shift	φ	$\pi/2$
Switching frequency	f_{s}	10 kHz
Blanking time	t_{bl}	800 ns

as shown in Fig. 8. The control signals for each transistor are generated by a dSPACE control platform. The tank is implemented by two 47 µH inductors and a 30 µF capacitor, all connected in series, with a total parasitic resistance of 10 mΩ. Finally, the load is a single 22-Ω high-power resistor.

This prototype has been tested under the same conditions of Fig. 9. The experimental results presented in Fig. 10 closely match the simulation results depicted in Fig. 9. The leg voltages v_{A} and v_{B} show a negative slope when connected to the highest dc-link level, possibly due to a high impedance of the cables connecting the batteries to the converter. The battery currents also show good correlation with the simulation waveforms except for a slight increase in current ripple. Other minor differences found in the experimental results can be attributed to unmatched values of the parasitic elements of the circuit, the blanking time required by the transistors (not included in the simulations), and inaccuracies in the measurements. Nonetheless, the average battery currents present only a 3.49% deviation among them, validating experimentally the operation of the converter under balanced conditions.

The simulation results presented in Figs. 11 and 12 evaluate the converter capability to precisely control the average neutral point currents $I_{2\text{A}}$ and $I_{3\text{A}}$, that in turn control the balance between the battery currents i_{BA1}, i_{BA2} and i_{BA3}. For the sake of simplicity and due to symmetry, only side-A control parameters have been modified during these simulations.

In Fig. 11, the control is activated to force $i_{2\text{A}} < 0$ by setting $k_{2\text{A}} = 0.2$. This action creates an unbalance in the battery module currents, with $I_{\text{BA1}} < I_{\text{BA2}}$. In Fig. 11(a), the control is restricted to operate only with active power ($s_{\text{A}}^{\text{P}} = 1$, $s_{\text{A}}^{\text{Q}} = 0$) and battery module BA1 delivers 16.27% less

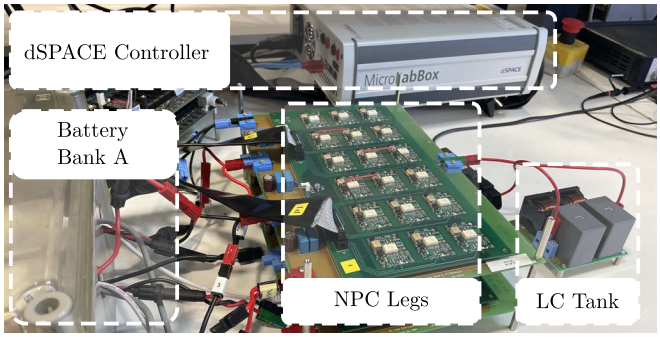

Fig. 8. Experimental hardware prototype.

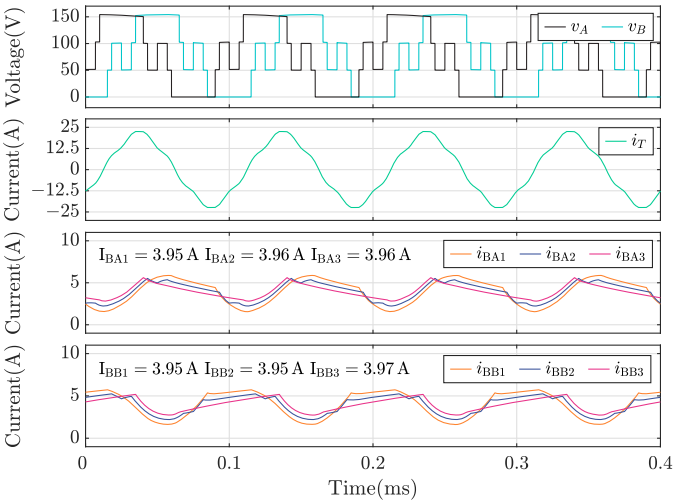

Fig. 9. Simulation results under balanced conditions, with control parameters $k_{2\text{A}} = k_{3\text{A}} = k_{2\text{B}} = k_{3\text{B}} = 0$, $m_{\text{A}} = m_{\text{B}} = 0.9$, phase shift $\varphi = \pi/2$.

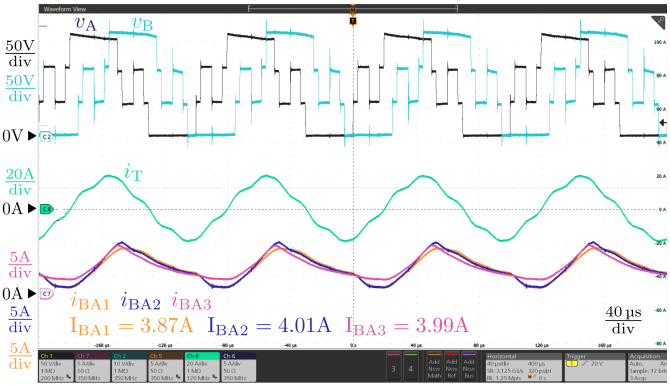

Fig. 10. Experimental results under the same conditions of Fig. 9.

current than modules BA2 and BA3. In Fig. 11(b), the control is restricted to operate only with reactive power ($s_{\text{A}}^{\text{P}} = 0$, $s_{\text{A}}^{\text{Q}} = 1$) and battery module BA1 delivers 18.28% less current than modules BA2 and BA3. In Fig. 11(c), where the full control is activated ($s_{\text{A}}^{\text{P}} = 1$ and $s_{\text{A}}^{\text{Q}} = 1$), the active and reactive power is employed to reduce battery module BA1 current by 30.28%. In all cases, the tank current is not significantly modified and the control action in one battery bank does not significantly affect the other battery bank.

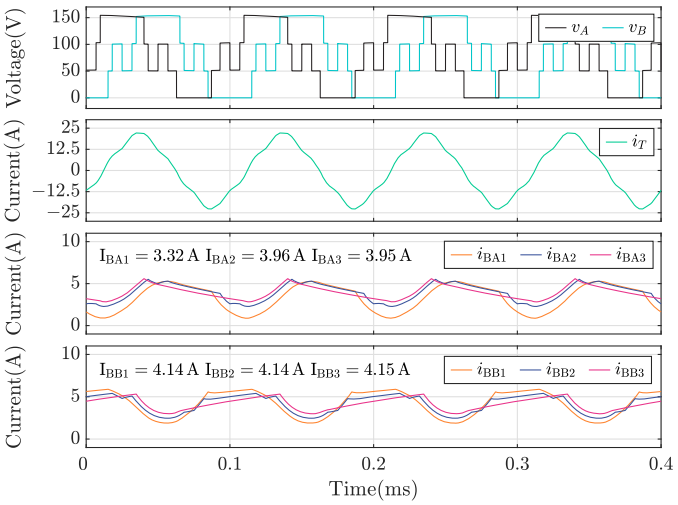

(a)

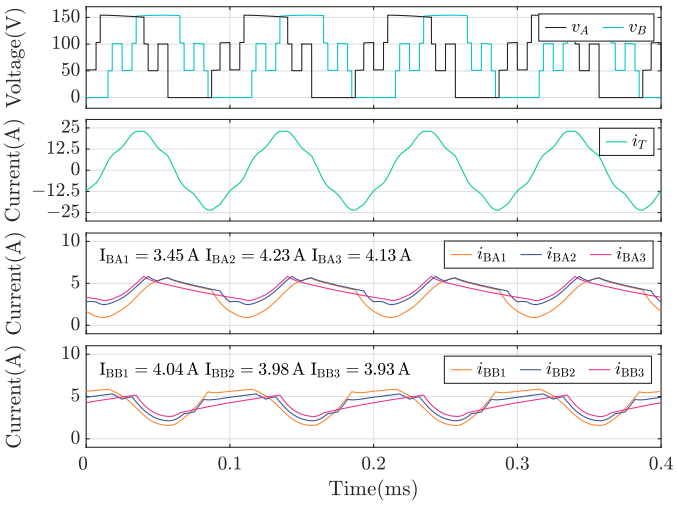

(b)

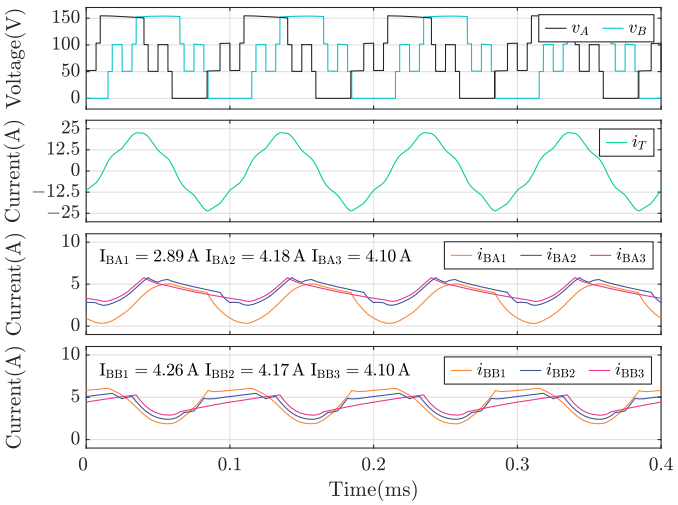

(c)

Fig. 11. Simulation results under unbalanced conditions, where $i_{2A} < 0$ is forced by setting $k_{2A} = 0.2$ and $k_{3A} = 0$. Conditions: $m_A = m_B = 0.9$ and $\varphi = \pi/2$. (a) Control based on active power. (b) Control based on reactive power. (c) Control based on both active and reactive power.

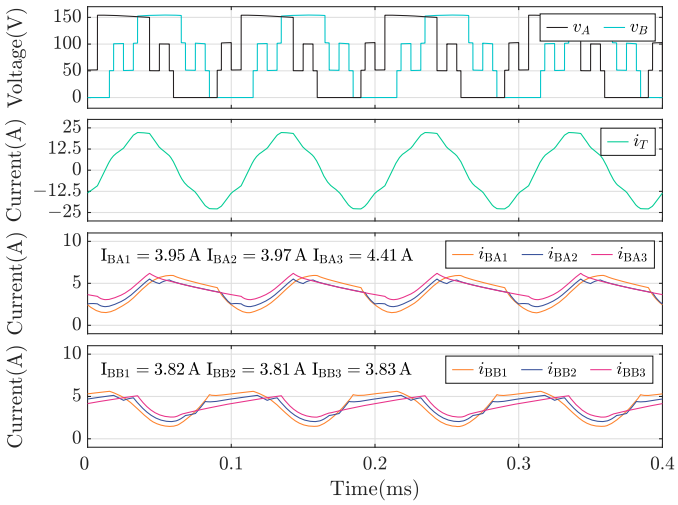

(a)

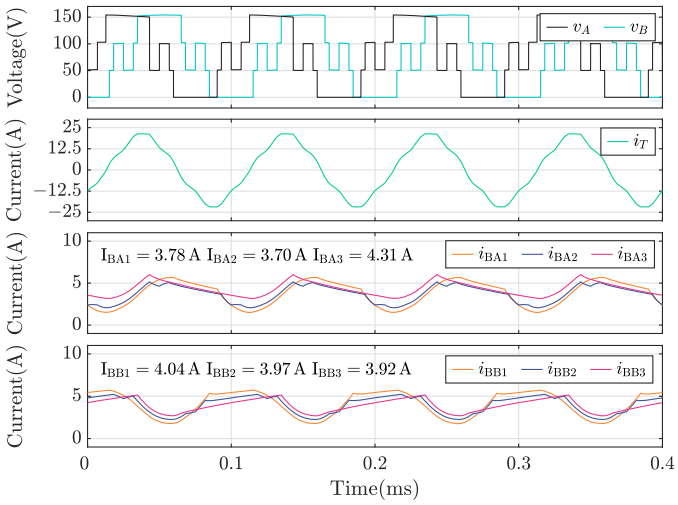

(b)

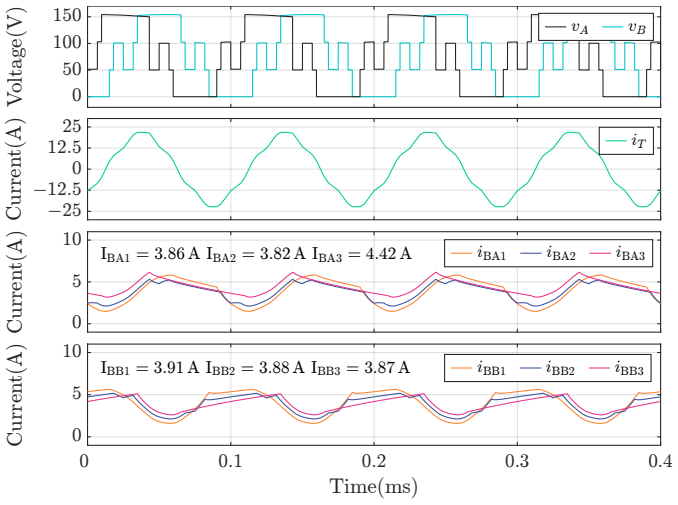

(c)

Fig. 12. Simulation results under unbalanced conditions, where $i_{3A} < 0$ is forced by setting $k_{2A} = 0$ and $k_{3A} = -0.2$. Conditions: $m_A = m_B = 0.9$ and $\varphi = \pi/2$. (a) Control based on active power. (b) Control based on reactive power. (c) Control based on both active and reactive power.

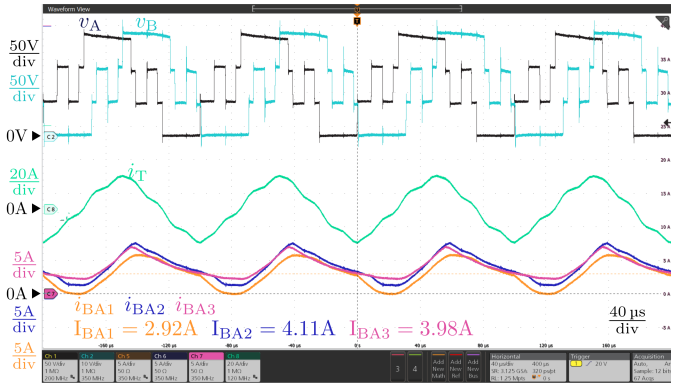

Fig. 13. Experimental results in the same conditions of Fig. 11(c).

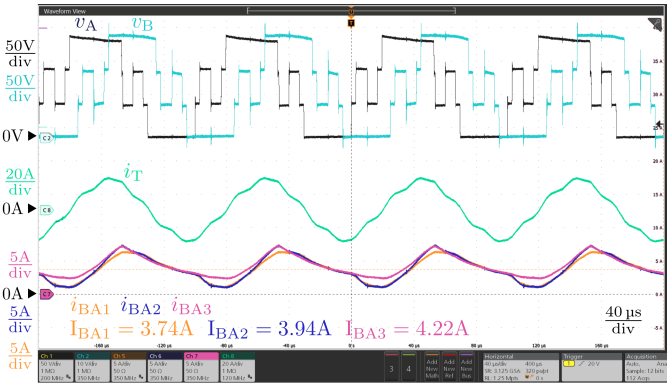

Fig. 14. Experimental results in the same conditions of Fig. 12(c).

In Fig. 12, the control is activated to force $i_{3A} < 0$ by setting $k_{3A} = -0.2$. This action creates an unbalance in the battery module currents, with $I_{BA2} < I_{BA3}$. In Fig. 12(a), the control is restricted to operate only with active power and battery module BA3 delivers 11.08% more current than the other two modules. In Fig. 12(b), the control is restricted to operate only with reactive power and battery module BA3 delivers 15.09% more current than the other two modules. In Fig. 12(c), where the full control is activated, battery module BA3 delivers 14.96% more current than the other two modules. In this case, the regulation is limited due to angle α_{b1} reaching the limit value of α_{b2}. This limitation in the regulation margin can be relaxed if the modulation index is reduced.

Figs. 13 and 14 present experimental results obtained in similar conditions to Figs. 11(c) and 12(c), respectively. In Fig. 13, a reduction in battery module BA1 current of 27.32% is achieved. However, in Fig. 14, the control action is further limited by the converter blanking time, which reduces the already saturated control action observed in the simulations. Due to this, the battery module BA3 current is only 9.9% higher than the other battery module currents.

V. Conclusions

In the context of developing modular and scalable hybrid batteries, this article has introduced a hybrid battery configuration consisting of two different battery banks, each formed by three series-connected battery modules, and a bidirectional four-level NPC dc-dc power converter to interface the two battery banks. The proposed circuit is simple and compact, employing only two NPC legs, one inductor, and one capacitor. Power processing losses are minimized by interfacing the highest-power-rated battery bank to the load, and then interfacing the other battery bank through the multilevel power converter. A novel modulation strategy and closed-loop control has been conceived to operate the proposed system and regulate the battery module currents. The regulation takes advantage of both the active power and reactive power being transferred. The power delivery of each of the three series-connected modules of each battery bank can be adjusted on demand, which enables a lossless battery module SoC balancing. The good performance of the proposed system has been verified through simulation and experiments, and other hybrid batteries configured with different number of levels (2, 3 or 4) in each side appear to also be feasible, using the same operating principle, modulation strategy, and closed-loop control strategy, as those presented here together with those of a previous publication focused on a three-level system. The control offers a reasonable regulation margin for the control of the battery module currents, even under high modulation indices. The regulation margin might be expanded if the modulation index is reduced.

References

[1] L. Amperex Technology Co. (2024, Oct.) CATL unveils freevoy super hybrid battery. [Online]. Available: https://www.catl.com/en/news/6301.html

[2] F. Naseri, C. Barbu, and T. Sarikurt, "Optimal sizing of hybrid high-energy/high-power battery energy storage systems to improve battery cycle life and charging power in electric vehicle applications," *Journal of Energy Storage*, vol. 55, p. 105768, 2022.

[3] X. Yuan, "Ultimate generalized multilevel converter topology," *IEEE Transactions on Power Electronics*, vol. 36, no. 8, pp. 8634–8639, Aug 2021.

[4] G. Garcia-Rojas, S. Busquets-Monge, A. Filba-Martinez, T. Sarikurt, S. Alepuz, and J. Bordonau, "Ev hybrid battery with integrated multilevel neutral-point-clamped interfacing and lossless intermodule state-of-charge balancing," *IEEE Open Journal of the Industrial Electronics Society*, vol. 6, pp. 130–144, 2025.

[5] I. Spina, G. Brando, and A. Dannier, "Minimizing the battery losses in mmc via zero-sequence voltage injection: an open challenge," in *2024 International Symposium on Power Electronics, Electrical Drives, Automation and Motion (SPEEDAM)*, June 2024, pp. 460–467.

[6] Y. Huang, F. Liu, Y. Zhuang, X. Diao, Y. Lei, and H. Zhu, "Bidirectional three-port converter for modular multilevel converter-based retired battery energy storage systems," *IEEE Transactions on Power Electronics*, vol. 39, no. 9, pp. 11 148–11 163, Sep. 2024.

[7] S. Busquets-Monge, A. Filba-Martinez, S. Alepuz, and A. Calle-Prado, "A modulation strategy to operate multilevel multiphase diode-clamped and active-clamped dc–ac converters at low frequency modulation indices with dc-link capacitor voltage balance," *IEEE Transactions on Power Electronics*, vol. 32, no. 10, pp. 7521–7533, 2017.

[8] S. Busquets-Monge, A. Filba-Martinez, S. Alepuz, J. Nicolas-Apruzzese, A. Luque, A. Conesa-Roca, and J. Bordonau, "Multibattery-fed neutral-point-clamped dc–ac converter with soc balancing control to maximize capacity utilization," *IEEE Transactions on Industrial Electronics*, vol. 67, no. 1, pp. 16–27, 2020.